Angewandte Chemie
Eine Zeitschrift der Gesellschaft Deutscher Chemiker

Supporting Information

A Pseudotetrahedral Terminal Oxoiron(IV) Complex: Mechanistic Promiscuity in C–H bond Oxidation Reactions

*Katrin Warm, Alice Paskin, Uwe Kuhlmann, Eckhard Bill, Marcel Swart, Michael Haumann, Holger Dau, Peter Hildebrandt, and Kallol Ray**

anie_202015896_sm_miscellaneous_information.pdf

Table of Contents

SUPPORTING INFORMATION

Experimental Procedures

Chemicals, materials and instrumentation

Chemicals and handling. The chemicals employed were purchased from the companies ABCR, ACROS, SIGMA-ALDRICH and TCI, and used without further purification. Anhydrous solvents (acetonitrile, diethylether, dichloromethane and acetone) were purchased from CARL-ROTH GmbH under the tradename ROTIDRY (>99.5%, < 50 ppm H_2O), degassed by freeze-pump-thaw methods prior to use and stored over activated molecular sieves. Deuterated solvents were purchased from EURISO-TOP.

Preparation and handling of air or water sensitive compounds were performed under an inert atmosphere using either Schlenk techniques or a glovebox OMNI-LAB 2 from VAC-ATMOSPHERES filled with N_2. Nitrogen and Argon of quality 5.0 were used for this purpose and were purchased from AIR LIQUIDE.

Elemental analysis. All elemental analyses were performed by the analytical service of the Institut für Chemie of the Humboldt-Universität zu Berlin. The percentages of Carbon, Hydrogen, Nitrogen and Sulphur were determined using an HEKAtech EURO EA 3000 analyzer. The reported values are the result of an average of two independent measurements except for Fluorine analysis, where only one measurement was performed.

Nuclear magnetic resonance spectroscopy. All NMR spectra were recorded using a BRUKER 300 DPX spectrometer equipped with a cryostat. Those of ^{1}H and ^{19}F nuclei were recorded in deuterated solvents, and chemical shifts (ppm) referenced against residual protic solvent peaks.

Electrospray ionization mass spectrometry. ESI-MS spectra of organic molecules and inorganic complexes in solution were recorded by using an ADVION EXPRESSION CMS spectrometer (under “typical” ionization conditions) and spectra in positive and negative mode were collected in parallel; acetonitrile was used as an eluent. For thermally unstable complexes, the freshly thawed solutions were directly injected into the instrument while the ionization source temperature was decreased to 50°C. The analysis of the data was carried out with the ADVION DATA EXPRESS Version 6.0.11.3.

Gaschromatography. GC analysis was carried out by using an AGILENT 7890B gas chromatograph (HP5 25 column, 30 m) with a flame-ionization detector. GC-MS was performed on an AGILENT 5977B spectrometer with a triple-axis detector.

Single crystal X-ray structure determinations. For the determination of the X-ray crystal structure of the complex data collection was performed at 100K on a BRUKER D8 VENTURE diffractometer by using Mo Kα radiation (λ = 0.71073 Å). Multi-scan absorption corrections implemented in SADABS[1] were applied to the data. The structure was solved by intrinsic phasing method (SHELXT 2014/5)[2] and refined by full matrix least square procedures based on F_2 with all measured reflections (SHELXL-2018/3)[3] in the graphical user interface SHELXle[4]) with anisotropic temperature factors for all non-hydrogen atoms. All hydrogen atoms were added geometrically and refined by using a riding model.
CCDC 2046107 contains the supplementary crystallographic data for this paper. These data can be obtained free of charge from the Cambridge Crystallographic Data Centre via www.ccdc.cam.ac.uk/data_request/cif.

Mössbauer spectroscopy. Mössbauer spectra in the absence of magnetic field were recorded on a SEECO MS6 spectrometer that comprises the following instruments: a JANIS CCS-850 cryostat, including a CTI-CRYOGENICS closed cycle 10K refrigerator, and a CTI-CRYOGENICS 8200 helium compressor. The cold head and sample mount are equipped with calibrated DT-670-Cu-1.4L silicon diode temperature probes and heaters. Temperature is controlled by a LAKESHORE 335 temperature controller. Spectra are recorded using a LND-45431 Kr gas proportional counter with beryllium window connected to the SEECO W204 γ-ray spectrometer that includes a high voltage supply, a 10 bit and 5 µs ADC and two single channel analyzers. Motor control and recording of spectra is taken care of by the W304 resonant γ-ray spectrometer. For the reported spectra a RIVERTEC MCO7.114 source (^{57}Co in Rh matrix) with an activity of about 1 GBq was used. All spectra were recorded in a plastic sample holder with a frozen solution sample at 35 K and data were accumulated for about 24 hours.
Applied-field Mössbauer spectra were recorded on a conventional spectrometers with alternating constant acceleration of the γ-source. The sample temperature was maintained constant in a closed-cycle Mössbauer magnet cryostat from Cryogenic Ltd. The latter is a split-pair super-conducting magnet system for applied fields up to 7 T. The temperature of the sample can be varied in the range 1.7 K to 300 K. The field at the sample is perpendicular to the γ-beam. The ^{57}Co/Rh source (1.8 GBq) was positioned at room temperature inside the gap of the magnet system at zero-field position, by using a re-entrant bore tube. The detector was a Si-Drift diode (150 mm^2 SDD CUBE) of a AXAS-M1 system from Ketek GmbH with vacuum-tight 200 mm stainless steel finger, which was inserted into the cryostat to position the diode also in the gap of the magnet. Isomer shifts are quoted relative to iron metal at 300 K, and the minimum experimental line width was 0.3 mm/s (full width at half-height). The magnetic Mössbauer spectra were simulated with the program *mx.SL* (by E.B.) by diagonalization of the spin Hamiltonian for electronic spins S = 2

$$\hat{H}_S = D\,[\hat{S}_z^2 - \frac{1}{3}S(S+1) + \frac{E}{D}(\hat{S}_x^2 - \hat{S}_y^2)] + \mu_B \vec{B}\cdot g \cdot \hat{\vec{S}} \qquad (1)$$

where *g* is the electronic *g* matrix, and *D* and *E/D* are the axial zero-field splitting and rhombicity. The hyperfine interaction for ^{57}Fe was calculated with the usual nuclear Hamiltonian parameterized by the hyperfine coupling matrix A and the usual terms for electric quadrupole interaction; isomer shifts were taken from additive ref. 5.[5]

X-ray absorption spectroscopy. XAS at the Fe K-edge was performed at beamline KMC-3 at the BESSY-II synchrotron (Helmholtz Center Berlin, Germany) as described earlier[6] using a set-up including a Si[111] double-crystal monochromator, a 13-element energy-resolving Si-drift detector (RaySpec) for X-ray fluorescence monitoring, and DXP-XMAP pulse-processing electronics (XIA). Samples were held at 20 K in a liquid-helium cryostat (Oxford). The energy axis of the monochromator was calibrated (accuracy ±0.1 eV) using the K-edge spectrum of an iron metal foil (fitted reference energy of 7112 eV in the first derivative spectrum). The spot size on the samples was ca. 1.5 x 3.0 mm (vertical x horizontal) as set by a focusing mirror and slits. X-ray fluorescence spectra were collected using a continuous scan mode of the monochromator (scan duration ~10 min). Up to 6 scans were averaged (1-2 scans per sample spot) for signal-to-noise ratio improvement. XAS data were processed (dead-time correction, background subtraction, normalization) to yield XANES and EXAFS spectra using our earlier described procedures and in-house software.[7] k^3-weighted EXAFS spectra were simulated with in-house software and phase functions from FEFF9 (S_0^2 = 0.8).[8] EXAFS simulation results are tabulated in Table S5.

Resonance Raman (rRaman). Resonance Raman spectra were measured in CD_2Cl_2 at –90 °C (Bruker cryostat) using 406 nm excitation form a Kr^+-laser at 5 mW power with a Horiba Jobin-Yvon LabRAM HR800 confocal Raman spectrometer. The sample concentrations employed were 4 mM.

Synthesis

tBu_3tacn. The tBu_3tacn ligand was synthesized following the procedure previously reported by Scarborough *et al.* [9] with slight modifications in the final step of the synthesis which are described here: Under inert conditions 1,4,7-tri-tert-butyl-1,4,7-triazacyclononane-2,6-dione (290 mg, 0.892 mmol) were added in small portions to 2.7 mL of a commercial solution of $LiAlH_4$ (1M in Et_2O; 3.0 eq) at 20 °C while stirring. The previously clear solution slowly turned turbid and was left to stir over night. Afterwards, the reaction mixture was cooled to 0°C and carefully quenched by the dropwise addition of dist. water. When no more gas development was observed the aqueous phase (ca 15 mL) was extracted 5 times with about 10 mL of Et_2O. The organic phases were collected, dried over $MgSO_4$ and the solvent was removed. After recrystallization from hot EtOH, the product was obtained as colourless crystalline needles (240 mg, 0.807 mmol, 90%). ^{1}H-NMR (300 MHz, $CDCl_3$): δ = 2.64 (s, 12H), 1.00 (s, 27H) ppm.

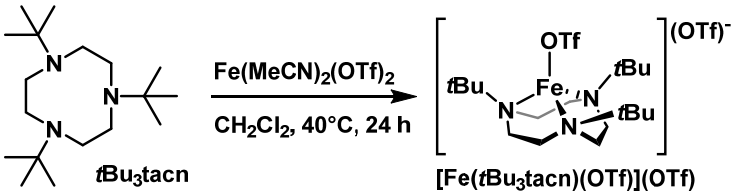

*t*Bu$_3$tacn [Fe(*t*Bu$_3$tacn)(OTf)](OTf)

[(tBu_3tacn)Fe(OTf)](OTf) (1). tBu_3tacn (60 mg, 0.20 mmol) was added to a suspension of $Fe(MeCN)_2(OTf)_2$ (79 mg, 0.18 mmol) in 2 mL DCM under an inert atmosphere at 20 °C and stirred for 26 h. The light brown suspension was filtered to remove the brown precipitate formed in the reaction and precipitated by the addition of Et_2O. The white solid formed was isolated and dried under vacuum over night (105 mg, 0.161 mmol, 88%). Crystals suitable for X-ray diffraction analysis were grown by diffusion of Et_2O into a solution of the complex in DCM at -40°C. ^{1}H-NMR (CD_2Cl_2, 300 MHz): 221.3 (br s), 48.0 (br s), -40.8 (br s) ppm; ^{19}F-NMR (CD_2Cl_2, 282 MHz): -66.2 (s) ppm; CHNS analysis: exp.: C: 35.79, H: 5.84, N: 6.28, S: 9.20, calc.: C: 36.87, H: 6.03, N: 6.45, S: 9.84. ESI-MS (MeCN, pos. mode): $[Fe(tBu_3tacn)Cl]^+$ *m/z* calc. 388.2; found 388.2.

2-(*tert*-butylsulfonyl)-iodosylbenzene (^{s}PhIO). ^{s}PhIO was synthesized according to previously reported procedures.[10] The ^{18}O-labelled ^{s}PhI^{18}O was synthesized as follows: A 1 M solution of $Na^{18}OH$ was prepared by the addition of NaH (40 mg, 1 mmol) to $H_2{}^{18}O$ under an inert atmosphere. 2-(tert-butylsulfonyl)(diacetoxyiodo)benzene (300 mg, 0.7 mmol) was added in small portions and the mixture was stirred for 30 min at 20 °C. The aqueous phase was removed by filtration through Teflon-tubes and washed with 0.5 mL portions of $H_2{}^{18}O$ until the pH was neutral. The pale yellow solid was then washed twice with anhydrous Et_2O and dried under vacuum (186 mg, 0.56 mmol, 80%). ^{1}H-NMR (300 MHz, $CDCl_3$): δ = 8.11 (d, J = 7.8 Hz, 1H), 7.90 – 7.80 (m, 2H), 7.66 – 7.58 (m, 1H), 1.41 (s, 9H) ppm.

***h*$_2$,*d*$_6$-cyclohexa-1,4-diene (*h*$_2$,*d*$_6$-1,4-CHD).** d_6-benzene (3.7 mL, 42 mmol), d_6-ethanol (7.0 mL, 120 mmol) and diethylether (12 mL) were added to 75 mL of liquid, anhydrous ammonia (NH_3) at –40 °C carefully. Subsequently, small portions of sodium metal (2.6 g, 113

mmol) were added over 4 h while maintaining the temperature at –40 °C. After the addition of each portion, the mixture was stirred until the dark blue colour had vanished before adding more sodium. The reaction mixture was left to warm to 20 °C slowly over night, then carefully quenched by the addition of water. The organic product was extracted 3x with decalin (20 mL each), the organic phases were collected, dried with $MgSO_4$ and the product was obtained by distillation. The crude product was purified by a second distillation and obtained as a colourless liquid (0.5 g, 6 mmol, 15%). The deuteration degree of the product was confirmed by ^{1}H- and ^{13}C-NMR spectroscopy. Purity of the compound (85%) was determined by ^{1}H-NMR by addition of a known amount of 1,3,5-trimethoxybenzene as an internal standard to the NMR solution and comparison of the signal integrals.
^{1}H-NMR (300 MHz, $CDCl_3$): δ = 2.64 (d, J = 1.5 Hz, 2H) ppm;^{13}C-NMR (126 MHz, $CDCl_3$): δ = 124.1 (t, J = 24 Hz), 25.3 (t, J = 19 Hz) ppm.

Sample preparation

In a typical experiment, 2 mL of a solution of the Fe^{II} complex **1** in DCM was cooled to -90 °C in a UV-Vis quartz cuvette (10 mm pathlength) and a solution of 4 eq sPhIO, dissolved in 0.1 mL DCM, was injected into the solution. The formation of the intermediate **2** was monitored by UV-Vis following the bands at 356 nm and 780 nm. The samples were transferred into precooled sample holders as soon as the formation was complete. λ_{max} (ε_{max}): 356 nm (7500 $M^{-1}cm^{-1}$), 780 nm (150 $M^{-1}cm^{-1}$), ESI-MS (pos. mode): *m/z* [Fe(tBu_3tacn)O(OTf)]+ exp. 518.7; calc. 518.2.
Samples for XAS, EPR and Mössbauer spectroscopy were prepared in 2 mM concentration from a Fe^{II} solution in butyronitrile using a minimum amount of DCM to dissolve the oxidant. Samples for rRaman (4 mM) and ESI-MS (1 mM) were prepared in pure DCM. Samples for NMR (3.68 mM) were prepared in d_2-DCM containing 2% h_2-DCM. For determination of the magnetic susceptibility by Evans' method, a precooled capillary containing the same solvent mixture was inserted into the NMR tube.
GC-MS and NMR samples for analysis of the organic products were prepared by addition of substrate (5 eq for xanthene, DHA and 1,4-CHD, 20 eq for ethylbenzene, 100 eq for toluene) in 0.1 mL solvent to a 0.5 mM solution of **2** at -70 °C. After the decay of the 356 nm and the 780 nm bands were confirmed by UV-Vis spectroscopy, the solutions were warmed to room temperature, quenched by the addition of Na_2SO_3, a known amount of biphenyl was added as internal standard and the solutions were filtered through a short plug of silica and $MgSO_4$ to remove the metal complex and traces of water.

Kinetic studies

Reactivity studies were performed either at -70 °C or -90 °C with 0.25 or 0.5 mM concentrations of **2**. After addition of the substrates (>20 eq) to a preformed solution of **2** the decay of the 356 nm band was monitored over 250 s and fitted with pseudo-first order kinetics to obtain k_{obs} values. Plotting the k_{obs} values over several concentrations and fitting them linearly yielded k_2 values. The k_2 values were normalized by the number of equivalent H atoms (k_2') in order to correlate them to the bond dissociation energies (BDE) of the corresponding C-H bonds.
Hydrogen/Deuterium Kinetic isotope effects (KIEs) were determined as the ratio of the k_2 value measured for the substrate containing exclusively C-H bonds and the k_2 value obtained from the deuterated substrate. In the case of 1,4-CHD, the corresponding deuterated compound applied was h_2,d_6-1,4-CHD possessing 2 equivalent H and D atoms respectively. Consequently, the KIE was calculated by equation (2):

$$KIE = \frac{k_2(h_8-CHD)}{2 \cdot k_2(h_2,d_6-CHD) - k_2(h_8-CHD)} \quad (2)$$

Due to the comparably high KIE of the reaction, a reasonable KIE value could only be obtained taking the experimental standard deviation σ into account (compare Supporting Figure S10B: k_2(h_8-CHD) = 12.78 ± 0.61 $M^{-1}s^{-1}$; k_2(h_2,d_6-CHD = 5.68 ± 0.28 $M^{-1}s^{-1}$). Within the 3σ error range of the measured k_2 values, the KIE of the reaction was found to be approximately 5.2. Within the 2σ error range, the KIE was calculated to be 12.6 accordingly.This implies that the KIE possesses with 99.7% (3σ range) probability a value of 5.2 or above and with a 95.0% probability a value of 12.6 or above confirming a considerable contribution of tunnelling effects to the reaction pathway.

$$KIE = \frac{(12.78 - 3 \cdot 0.61)\ M^{-1}s^{-1}}{2 \cdot (5.68 + 3 \cdot 0.28)\ M^{-1}s^{-1} - (12.78 - 3 \cdot 0.61)\ M^{-1}s^{-1}} = \frac{10.95}{6.52 - 5.48} \approx 5.2$$

$$KIE = \frac{(12.78 - 2 \cdot 0.61)\ M^{-1}s^{-1}}{2 \cdot (5.68 + 2 \cdot 0.28)\ M^{-1}s^{-1} - (12.78 - 2 \cdot 0.61)\ M^{-1}s^{-1}} = \frac{11.56}{6.24 - 5.78} \approx 12.6$$

Computational details and theoretical methods

All coordinates and related data will be uploaded onto iochem-bd.org. All DFT calculations were performed with the Amsterdam Density Functional (ADF)[11] and QUILD[12] programs, and were performed using the unrestricted Kohn-Sham scheme. Molecular orbitals were expanded in an uncontracted set of Slater type orbitals (STOs) of triple-ζ quality with double polarization functions (TZ2P).[13] Core

electrons were not treated explicitly during the geometry optimizations (frozen core approximation[11b]). An auxiliary set of s, p, d, f, and g STOs was used to fit the molecular density and to represent the Coulomb and exchange potentials accurately for each SCF cycle. Geometries of all possible spin states were optimized with the QUILD[12] program using adapted delocalized coordinates until the maximum gradient component was less than 10^{-4} a.u. Energies, gradients and Hessians[14] (for vibrational frequencies) were calculated using S12g,[15] in all cases by including solvation effects through the COSMO[16] dielectric continuum model with appropriate parameters for the solvents.[17] For computing Gibbs free energies, all small frequencies were raised to 100 cm^{-1} in order to compensate for the breakdown of the harmonic oscillator model.[18] Scalar relativistic corrections have been included self-consistently in all calculations by using the zeroth-order regular approximation (ZORA).[19] For all calculations carried out with S12g the Becke[20] grid of VeryGood quality was used, except the calculations of the frequencies which were performed with a Becke grid of Normal quality.
All computational data will be uploaded (DOI:10.19061/iochem-bd-4-27) onto the IOCHEM-BD platform (www.iochem-bd.org)[21] to facilitate data exchange and dissemination, according to the FAIR principles[22] of OpenData sharing.

Results and Discussion

Spectroscopic studies

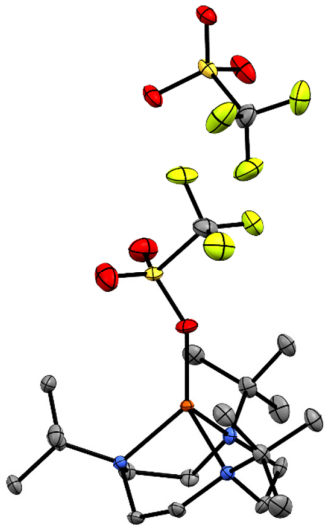

Figure S1. Molecular structure of one of the two crystallographically independent molecules of **1** obtained by XRD. Atoms are displayed as thermal ellipsoids at 50% probability level; H atoms are omitted for clarity. Structural parameters are summarized in Tables S1 and S2. (Atom types: Fe: orange; N: blue, C: grey; O: red; S: yellow; F: green.)

Table S1. Selected bond lengths and distances in the two crystallographically independent molecules of **1**.

Atoms	d [Å]	Atoms	Angles [°]
Fe1-N	2.1052(18) 2.1061(18) 2.1212(18)	N-Fe1-N	88.32(7) 86.51(7) 87.44(7)
Fe1-O	1.9223(16)	N-Fe1-O	125.89(8) 131.95(7) 122.93(8)
Fe2-N	2.1052(18) 2.1234(18) 2.1238(19)	N-Fe2-N	87.08(7) 87.65(7) 86.59(8)
Fe2-O	1.9349(17)	N-Fe2-O	136.25(7) 123.37(8) 121.36(8)

Table S2. Crystallographic Data for **1**.

Space group	P 2_1/n
Unit cell parameters	a = 18.3697(12) Å b = 13.8677(9) Å c = 22.2464(13) Å α = 90° β = 92.475(2)° γ = 90° V = 5661.9(6) Å^2
Z	8
Temperature	100(2) K
Total number of reflections collected (reflections with I > 2σ(I))	10416 (9566)
Number of parameters/restraints	717/95
θ_{min}, θ_{max}	2.35, 25.38°
F (0 0 0)	2720
Crystal dimensions [mm x mm x mm]	0.81 x 0.51 x 0.38
Absorption coefficient μ	0.759
h, k, l range	-22 < h < 22 -16 < k < 16 -26 < l < 26
R factor	0.0374
wR factor	0.0879
Goodness of Fit (GooF)	1.026

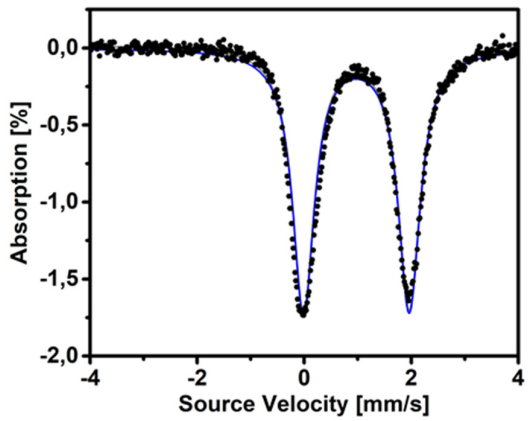

Figure S2. Zero-field Mössbauer spectrum of a solid sample of **1** at 15 K displaying an isomer shift of δ = 0.974 mm s^{-1} and quadrupole splitting of ΔE_Q = 1.976 mm s^{-1}).

Table S3. Comparison of selected spectroscopic properties of complex **1** and intermediate **2** calculated by DFT for S=0, S=1 and S=2 with the experimental values from XRD, EXAFS, Mössbauer and resonance Raman spectroscopy for **1** and **2**.

	1			Exp	**2**			Exp
Properties	S=0	S=1	S=2		S=0	S=1	S=2	
Rel. energy[a]	+36.96	+26.84	0.0		+4.29	-0.32	0.0	
Gibbs	+38.29	+26.54	0.0		+6.61	+0.82	0.0	
R (Fe-O) [Å]	1.950	1.947	1.945	1.92/1.94	1.540	1.586	1.627	1.66
R (Fe-N)^{av} [Å]	1.979	2.068	2.137	2.11	1.957	2.008	2.058	2.06
τ_4^{gen} [b]	1.017	0.964	0.954	1.00/0.97	1.017	0.864	0.790	
$\nu_{Fe=O}$ [cm^{-1}]	-	-	-		1004	949	893	802
δ [mm^{-1} s^{-1}]	0.723	0.856	0.913	0.974	-0.090	-0.023	0.064	0.11

a) obtained at OPBE/TZ2P in kcal/mol; b) based on τ_4 from DOI 10.1039/b617136b (see below)

The τ_4^{gen} parameter is based on the ideas by Houser and co-workers, who proposed a simple equation for getting a parameter τ_4 that goes from 1.00 for a perfect tetrahedral geometry to 0.00 for a perfect square planar geometry:

$$\tau_4 = \frac{360° - (\alpha + \beta)}{141}$$

Houser and co-workers proposed to choose "the two largest θ angles in the four-coordinate species", which is not specific enough. It should be generalized in the sense that for a tetra-coordinated metal with ligating atoms L1, L2, L3, L4, among the three possible pairs of angles:

Molecule A in X-ray structure

- **L1-M-L2, L3-M-L4 (N1-Fe-O) 131.95 (N2-Fe-N3) 86.51 Sum: 218.46**
- L1-M-L3, L2-M-L4 (N1-Fe-N2) 87.44 (N3-Fe-O) 125.89 Sum: 213.33
- L1-M-L4, L2-M-L3 (N1-Fe-N3) 88.32 (N2-Fe-O) 122.93 Sum: 211.25

Molecule B in X-ray structure

- L1-M-L2, L3-M-L4 (N1-Fe-O) 121.36 (N2-Fe-N3) 87.08 Sum: 208.44
- L1-M-L3, L2-M-L4 (N1-Fe-N2) 87.65 (N3-Fe-O) 123.37 Sum: 211.02
- **L1-M-L4, L2-M-L3 (N1-Fe-N3) 86.59 (N2-Fe-O) 136.25 Sum: 222.84**

the combination should be chosen which has the largest sum of θ angles. For instance for ^{XRAY}1, the angles are shown above, leading to a τ_4^{gen} value of 1.004 (molecule A in X-ray structure) and 0.973 (molecule B in X-ray structure).

Table S4. Comparison of the selected spectroscopic properties of TauD-***J***, intermediate **2,** various trigonal bipyramidal Fe^{IV}=O intermediates and the octahedral *S*=1 (TMC)Fe^{IV}=O intermediate.

Properties	TauD-J[23]	**2**	$(TMG_3tren)Fe^{IV}$=O[24]	$(TMG_2dien)(X)Fe^{IV}$=O X = MeCN[24]	$(TMG_2dien)(X)Fe^{IV}$=O X = N_3^- [24]	$(TMG_2dien)(X)Fe^{IV}$=O X = Cl^-[25]	$(H_3buea)Fe^{IV}$=O[26]	(MeCN)(TMC) Fe^{IV}=O[27]
λ_{max} [nm] (ε [M^{-1} cm^{-1}])	318	356 (7500) 780 (150)	400 (9800) 825 (260) 866 (250)	380 (2800) 805 (270)	412 (9700) 827 (290) 867 (275)	385 (7800) 803 (295) 825 (275)	350 (4200) 440 (3100) 550 (1900) 808 (280)	820 (400)
R (Fe-O) [Å]	1.62	1.66	1.65	1.65	-	1.65	1.680(1)	1.646(3)
$\nu_{Fe=O}$ [cm^{-1}]	821	802	843	807	833	810	798	834
δ [mm^{-1} s^{-1}]	0.31	0.11	0.09	0.08	0.12	0.08	0.02	0.17
ΔE_Q [mm^{-1} s^{-1}]	0.88	0.96	–0.29	0.58	–0.30	0.41	0.43	1.24
A_{xx}, A_{yy}, A_{zz} [T]		*S* = 1: –19.6, –4.6, –26.0 *S* = 2: –10.1, –3.3, –36.1	–15.5, –14.8, –28.0	–13.9, –15.8, –26.0	–15.5, –14.5, –27.0	–15.1, –15.4, –26.6	-	–22.6, –18.3, –2.9
E_o [eV]	7123.8	7123.2	7123.2	7123.6	7124.2	7123.9	-	7124.5
$E_{pre\text{-}edge}$ [eV]	-	7114.7, 7116.9	7113.8, 7115.6	7113.3, 7115.0	7113.8, 7115.7, 7118.1	7113.9, 7115.7	-	7114.1

SUPPORTING INFORMATION

Evans NMR spectroscopy

For determination of μ_{eff} of intermediate **2** by Evans NMR method, a solution of 2.75 mg of **1** (4.23 µmol) was dissolved in 1.00 mL of d_2-DCM containing 2% h_2-DCM. At -90 °C a solution of 5.4 mg ^{s}PhIO in 0.15 mL of the DCM mixture was added and the formation of the intermediate **2** was followed by UV-Vis spectroscopy. The solution (c = 3.68 mM) was filled into an NMR-tube and frozen. For the measurement, a precooled capillary containing the same DCM mixture as was used as solvent was inserted into the freshly melted solution and the NMR tube was directly inserted into the precooled NMR spectrometer and measured at -90 °C with a spectrometer radiofrequency F of 300 MHz.
The frequency difference between the h_2-DCM signals in the sample solution and in the pure solvent in the capillary (Δf = 64.02 Hz) was used to calculate the magnetic moment μ_{eff} according to formulas (3) and (4):

$\chi\_M = (3\,\Delta f)/(4\,\pi \cdot F \cdot c)$ (3)

$\mu_{eff} = \sqrt{8(\chi_M \cdot T)}$ (4)

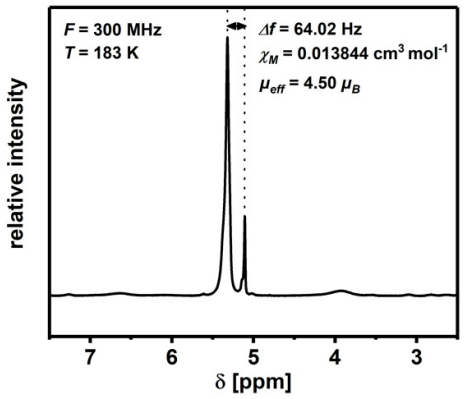

Figure S3. Zoom into the ^{1}H-NMR spectrum of **2** at the CH_2Cl_2 signal for the determination of the magnetic moment μ_{eff}.

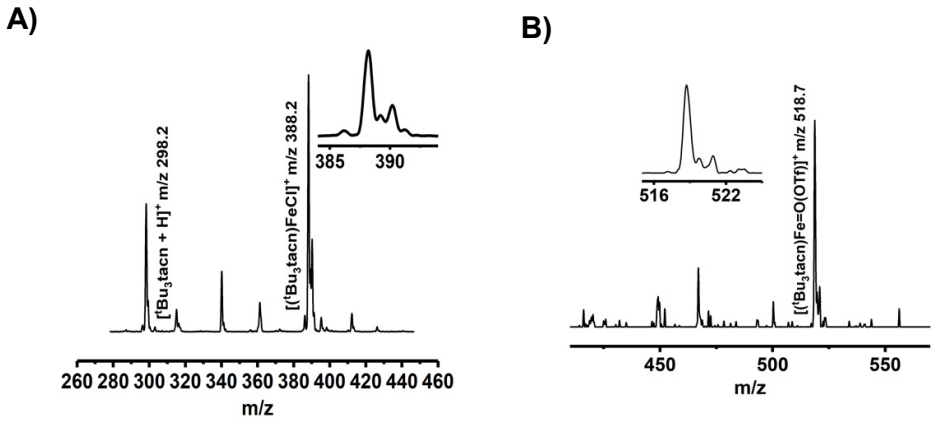

Figure S4. ESI-MS signals obtained for solutions of **1** under standard ionization conditions (left, inset shows zoom at *m/z* [Fe(tBu3tacn)Cl]$^+$ 388.2 (calc. 388.2)) and for a freshly melted solution of **2** measured with decreased capillary temperature (+50 °C) (right, inset shows zoom at *m/z* [Fe(tBu3tacn)(O)(OTf)]$^+$ 518.7 (calc. 518.2)).

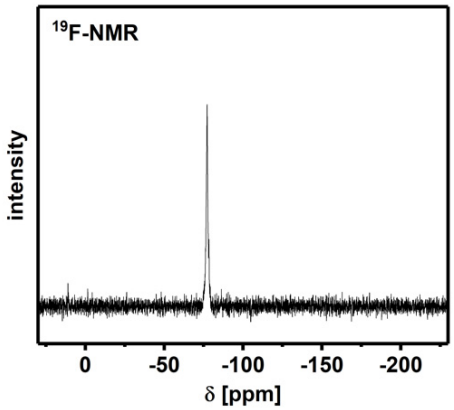

Figure S5. ^{19}F-NMR spectrum of **2** at -90 °C displaying one signal at -78 ppm corresponding to free triflate anion(s).

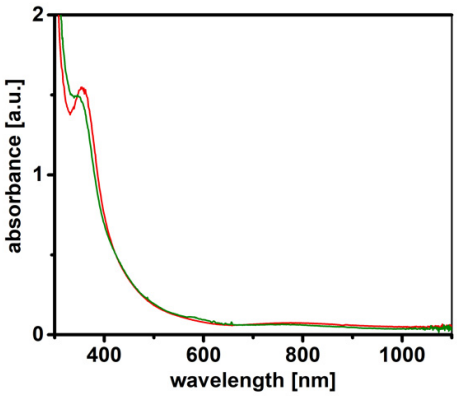

Figure S6. UV-Vis spectra of the reaction product of 0.25 mM **1** with 4 eq ^{s}PhIO at -90 °C in CH_2Cl_2 (red) and PrCN (green) solvents.

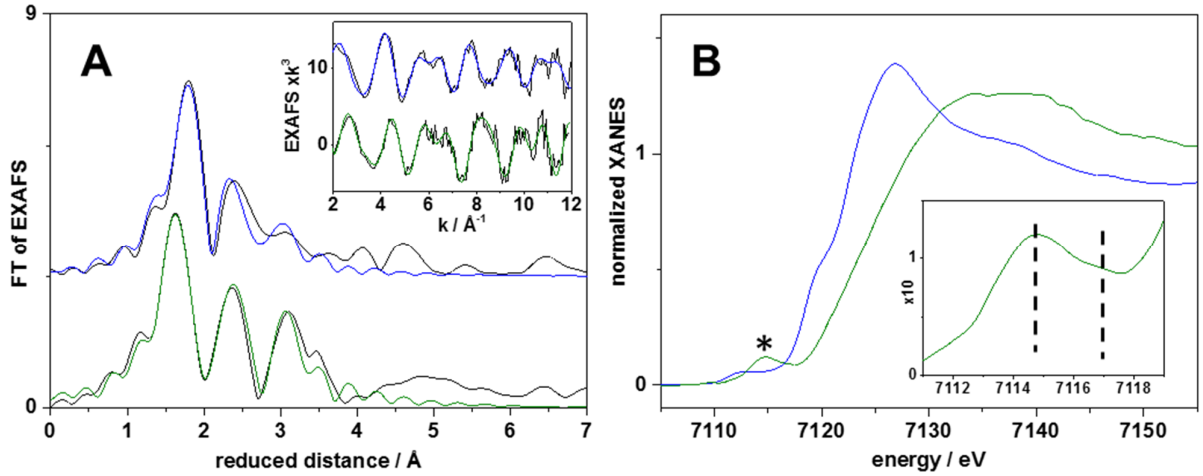

Figure S7. A) Fourier-transforms (FT) of the experimental extended X-ray absorption fine structure (EXAFS) data of **1** (blue) and **2** (green); the inset shows the k^3-weighted EXAFS spectra on a wavevector (k) scale (black lines, experimental data; colored lines, simulations with parameters in Table S5) B) Normalized X-ray absorption near edge structure (XANES) spectra of **1** (blue) and **2** (green) in a butyronitrile/DCM (10:1) solution featuring an edge energy (at 50 % level) of 7119.7 eV for **1** and 7123.2 eV for **2**; the inset shows 1s→3d pre-edge feature in the XANES (asterisk) of **2**, in which two spectral features around 7115 eV and 7117 eV (dashed lines) may tentatively be discernable.

Table S5. EXAFS fit parameters.

	shell	N [per Fe]	R [Å]	$2\sigma^2 \cdot 10^3$ [Å^2]	R_F (1-3 Å)
1	Fe-O	1.4	2.01	7	14.1%
	Fe-N	3[a]	2.19	2	
	Fe-C	3.6[c]	2.92	8[d]	
	Fe-C	5.4[c]	3.48	8[d]	
2	Fe=O	0.8[b]	1.66	2[a]	10.2%
	Fe-O	0.2[b]	1.98	2[a]	
	Fe-N	3[a]	2.06	7	
	Fe-C	3.5[c]	2.83	2[d]	
	Fe-C	5.5[c]	3.41	2[d]	

N, coordination number; R, interatomic distance; $2\sigma^2$, Debye-Waller factor; R_F, fit error sum. [a] Fixed parameters. [b,c] coupled to a sum of 1 or 9. [d] coupled to equal.

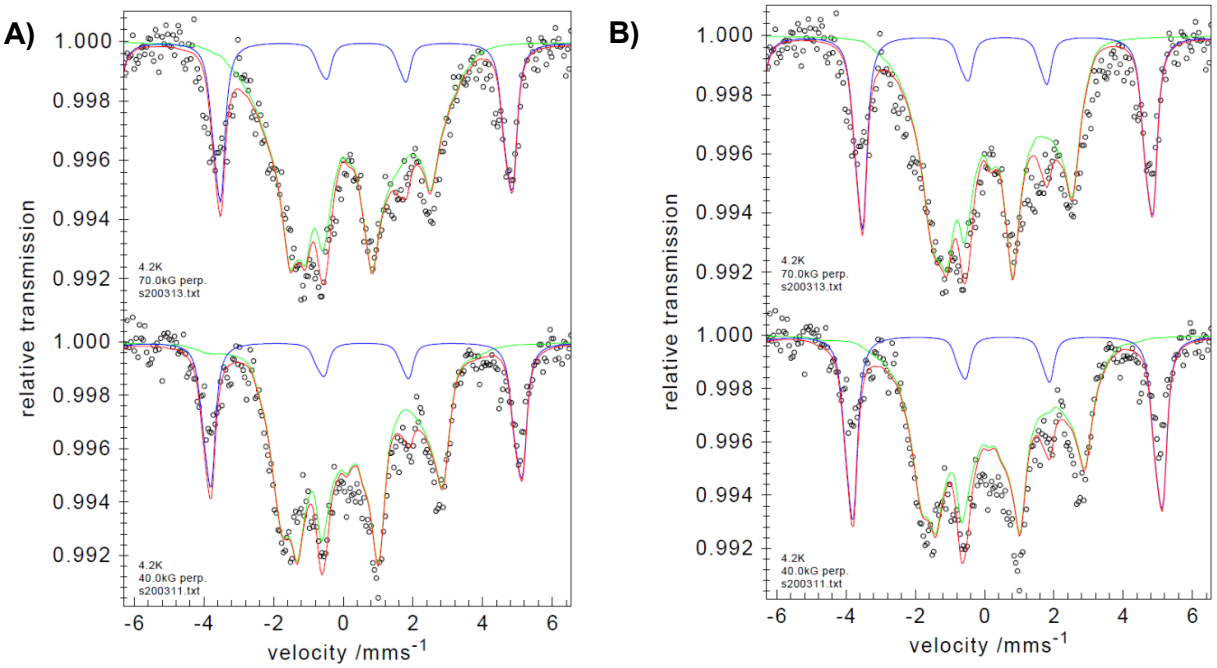

Figure S8. Magnetic field Mössbauer spectra of a frozen solution of **2** in butyronitrile/DCM (10:1) measured at 4.2 K applying a perpendicular magnetic field of 70.0 kG (top) or 40.0 kG (bottom); black circles: measured data, blue line: simulated spectra for an impurity, green line: simulated spectra for the Fe^{IV}=O species, red line: sum of the simulated spectra; A) simulation for an Fe^{IV} S = 2 system with isotope shift of δ = 0.10 mm s^{-1} and quadrupole splitting of ΔE_Q = 1.00 mm s^{-1}, g_x, g_y, g_z = 2.00, D = 5 cm^{-1}, E/D = -0.08, A_{xx} = -10.11 T, A_{yy} = -3.35 T, A_{zz} = -36.07 T; B) simulation for an Fe^{IV} S = 1 system with isotope shift of δ = 0.10(3) mm s^{-1} and quadrupole splitting of ΔE_Q = -1.00(5) mm s^{-1}, g_x, g_y, g_z = 2.00, D = 3.54 cm^{-1}, E/D = -0.30, A_{xx} = -19.63 T, A_{yy} = -4.65 T, A_{zz} = -26.0 T.

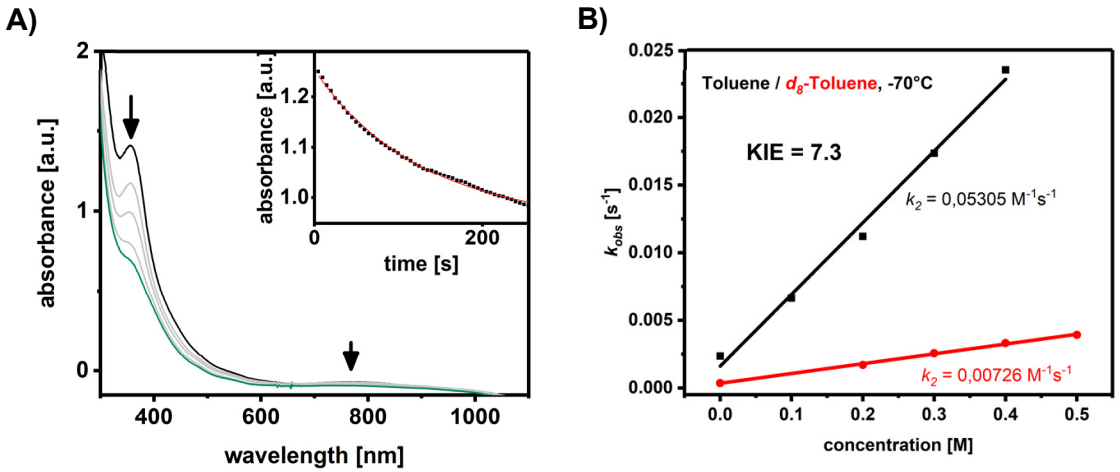

Figure S9. A) Changes in the UV-Vis absorption spectra of a 0.5 mM solution of **2** (black line) in CH_2Cl_2 at -70 °C upon addition of 600 eq toluene; inset shows time trace for the decay of the 356 nm band and its pseudo-first order fit. B) Plots of the pseudo-first order rate constants k_{obs} vs the substrate concentrations for toluene and d_8-toluene in order to determine the second-order rate constants k_2 and the kinetic isotope effect (KIE) value for the reaction of **2** with toluene.

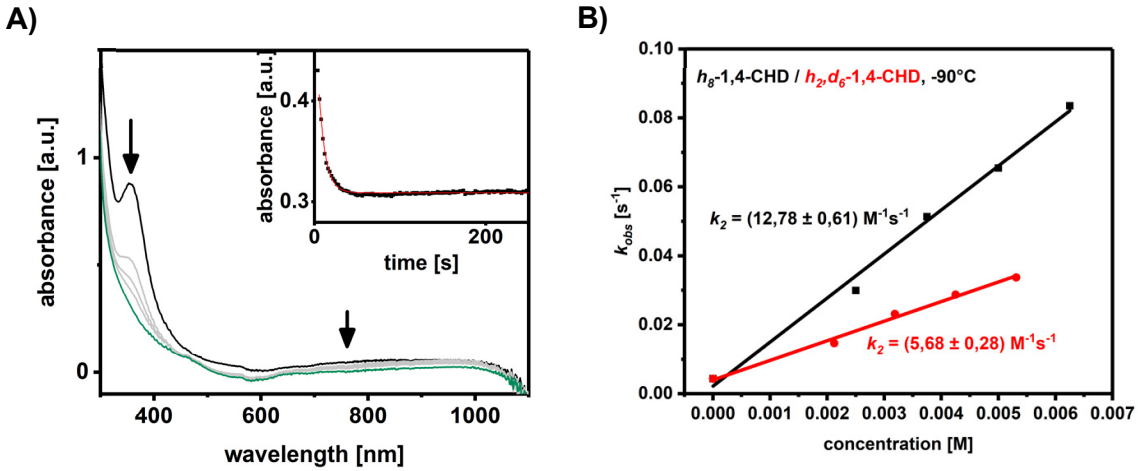

Figure S10. A) Changes in the UV-Vis absorption spectra of a 0.125 mM solution of **2** (black line) in CH_2Cl_2 at -90 °C upon addition of 50 eq cyclohexa-1,4-diene (1,4-CHD); inset shows time trace for the decay of the 356 nm band and its pseudo-first order fit. B) Plots of the pseudo-first order rate constants k_{obs} vs the substrate concentrations for 1,4-CHD and h_2,d_6-1,4-CHD in order to determine the second-order rate constant k_2 and the kinetic isotope effect (KIE) for the reaction of **2** with 1,4-CHD. The KIE of the reaction was approximated within the 2σ error range of the measured k_2 values as described in the beginning of this section.

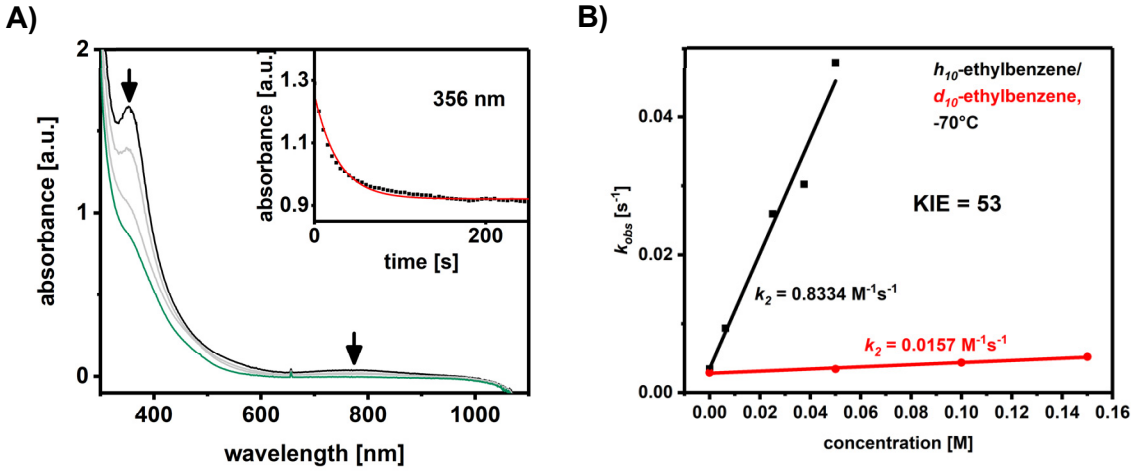

Figure S11. A) Changes in the UV-Vis absorption spectra of a 0.25 mM solution of **2** (black line) in CH_2Cl_2 at -70 °C upon addition of 200 eq ethylbenzene; inset shows time trace for the decay of the 356 nm band and its pseudo-first order fit. B) Plots of the pseudo-first order rate constants k_{obs} vs the substrate concentrations for ethylbenzene and d_{10}-ethylbenzene in order to determine the second-order rate constants k_2 and the kinetic isotope effect (KIE) value for the reaction of **2** with ethylbenzene.

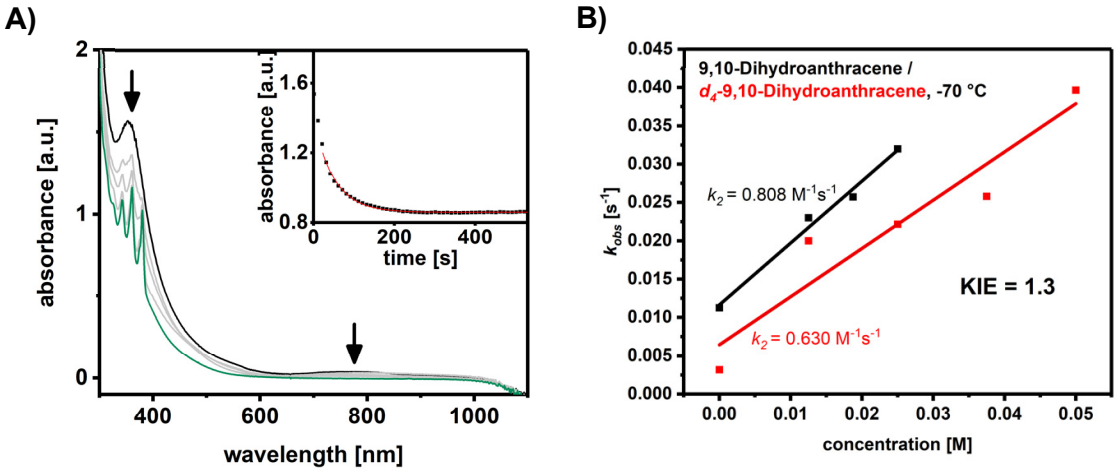

Figure S12. A) Changes in the UV-Vis absorption spectra of a 0.25 mM solution of **2** (black line) in CH_2Cl_2 at -70 °C upon addition of 75 eq 9,10-dihydroanthracene (DHA); inset shows time trace for the decay of the 351 nm band and its pseudo-first order fit. B) Plots of the pseudo-first order rate constants k_{obs} vs the substrate concentrations for DHA and d_4-DHA in order to determine the second-order rate constants k_2 and the kinetic isotope effect (KIE) value for the reaction of **2** with DHA.

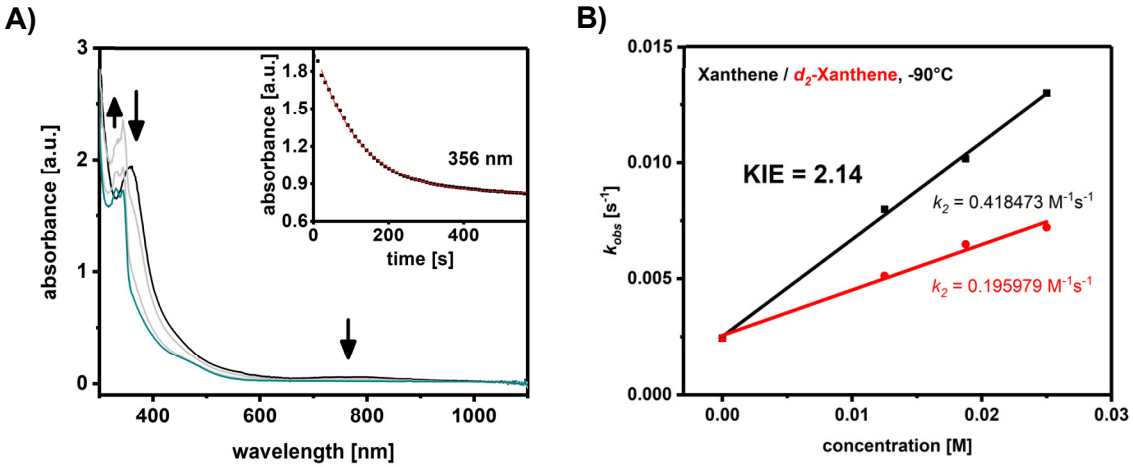

Figure S13. A) Changes in the UV-Vis absorption spectra of a 0.25 mM solution of **2** (black line) in CH_2Cl_2 at -90 °C upon addition of 50 eq xanthene; inset shows time trace for the decay of the 356 nm band and its pseudo-first order fit. B) Plots of the pseudo-first order rate constants k_{obs} vs the substrate concentrations for xanthene and d_2-xanthene in order to determine the second-order rate constants k_2 and the kinetic isotope effect (KIE) value for the reaction of **2** with xanthene.

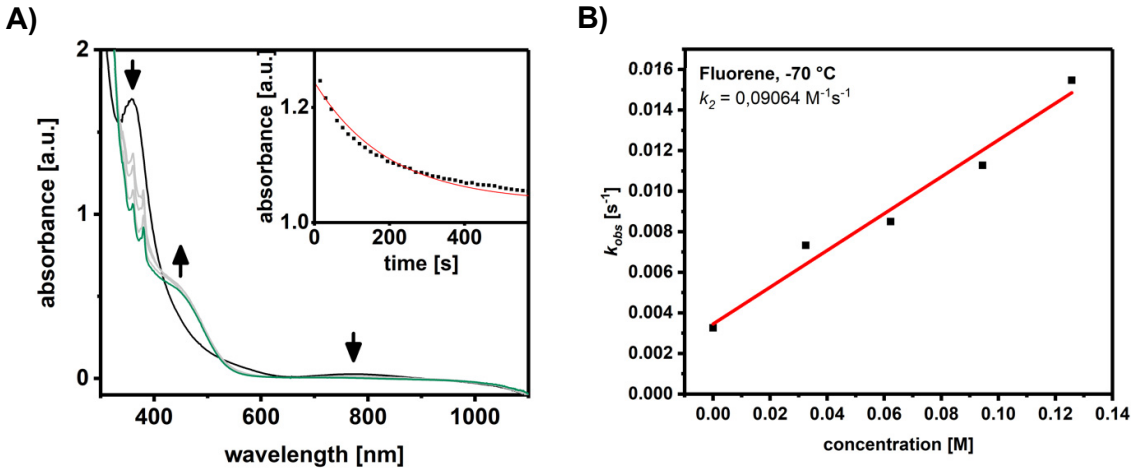

Figure S14. A) Changes in the UV-Vis absorption spectra of a 0.25 mM solution of **2** (black line) in CH_2Cl_2 at -70 °C upon addition of 500 eq fluorene; inset shows time trace for the decay of the 356 nm band and its pseudo-first order fit. B) Plots of the pseudo-first order rate constants k_{obs} vs the substrate concentrations for fluorene in order to determine the second-order rate constant k_2 for the reaction of **2** with fluorene.

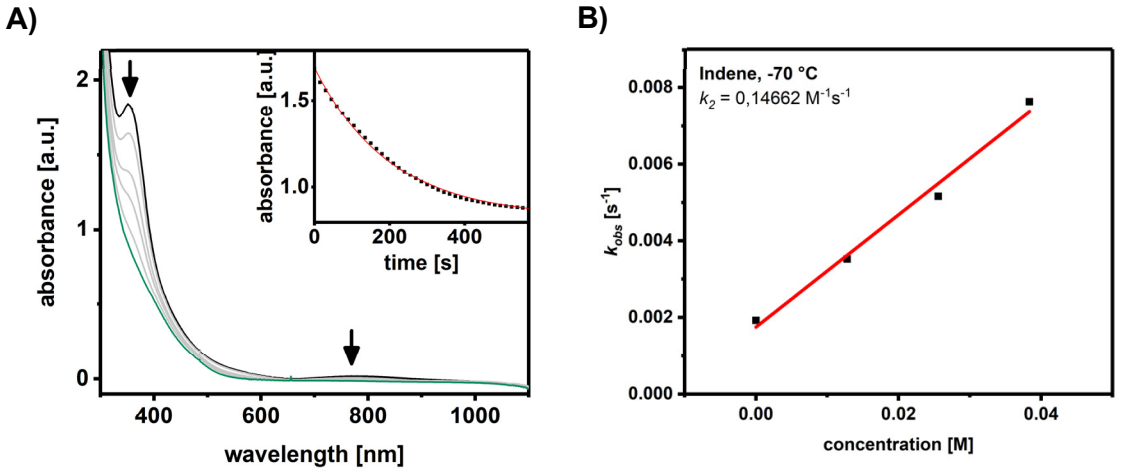

Figure S15. A) Changes in the UV-Vis absorption spectra of a 0.25 mM solution of **2** (black line) in CH_2Cl_2 at -70 °C upon addition of 100 eq indene; inset shows time trace for the decay of the 356 nm band and its pseudo-first order fit. B) Plots of the pseudo-first order rate constants k_{obs} vs the substrate concentrations for indene in order to determine the second-order rate constant k_2 for the reaction of **2** with indene.

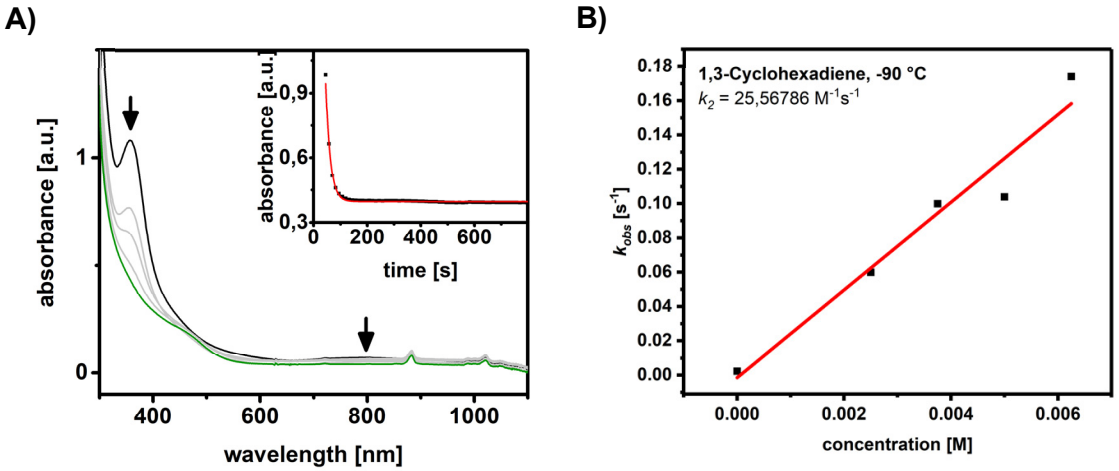

Figure S16. A) Changes in the UV-Vis absorption spectra of a 0.125 mM solution of **2** (black line) in CH_2Cl_2 at -90 °C upon addition of 25 eq cyclohexa-1,3-diene (1,3-CHD); inset shows time trace for the decay of the 356 nm band and its pseudo-first order fit. B) Plots of the pseudo-first order rate constants k_{obs} vs the substrate concentrations for 1,3-CHD in order to determine the second-order rate constant k_2 for the reaction of **2** with 1,3-CHD.

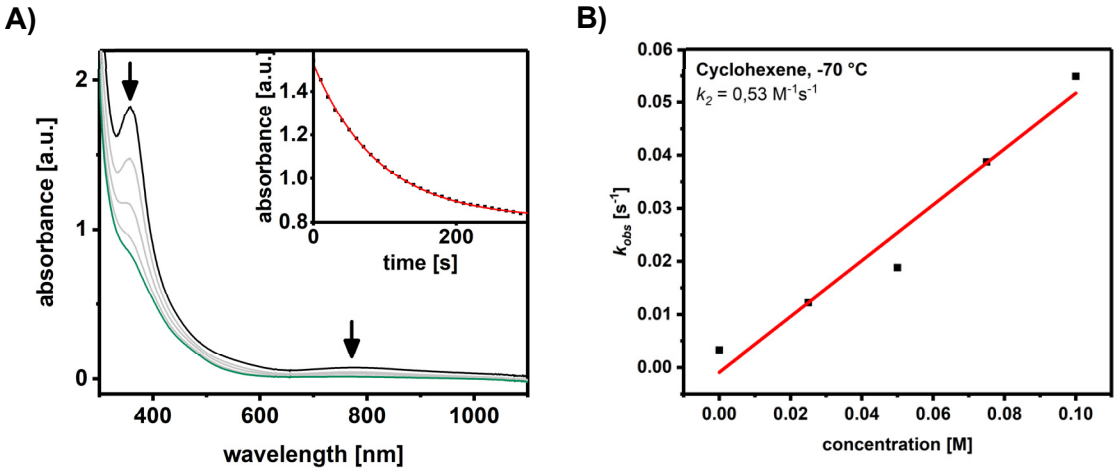

Figure S17. A) Changes in the UV-Vis absorption spectra of a 0.25 mM solution of **2** (black line) in CH_2Cl_2 at -70 °C upon addition of 100 eq cyclohexene; inset shows time trace for the decay of the 356 nm band and its pseudo-first order fit. B) Plots of the pseudo-first order rate constants k_{obs} vs the substrate concentrations for cyclohexene in order to determine the second-order rate constant k_2 for the reaction of **2** with cyclohexene.

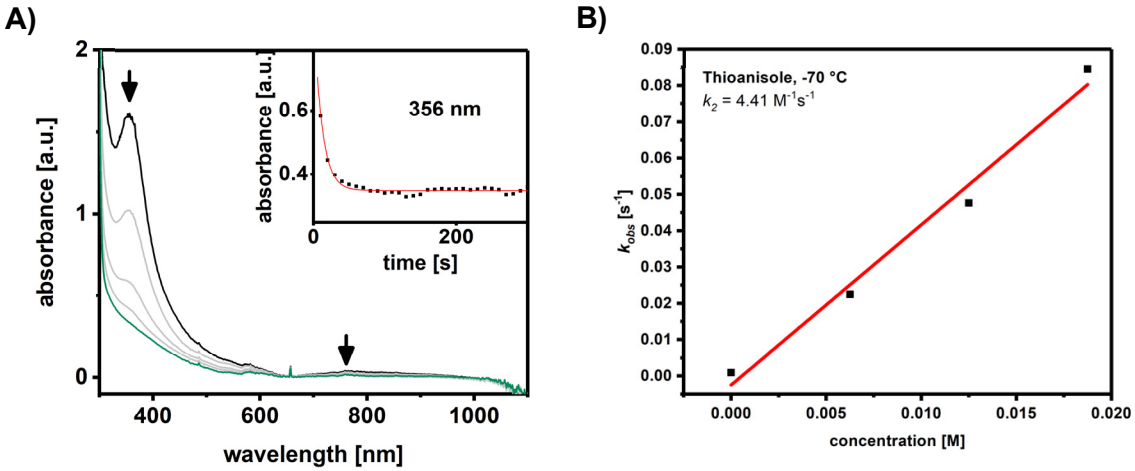

Figure S18. A) Changes in the UV-Vis absorption spectra of a 0.25 mM solution of **2** (black line) in CH_2Cl_2 at -70 °C upon addition of 75 eq thioanisole; inset shows time trace for the decay of the 356 nm band and its pseudo-first order fit. B) Plots of the pseudo-first order rate constants k_{obs} vs the substrate concentrations for thioanisole in order to determine the second-order rate constant k_2 for the reaction of **2** with thioanisole.

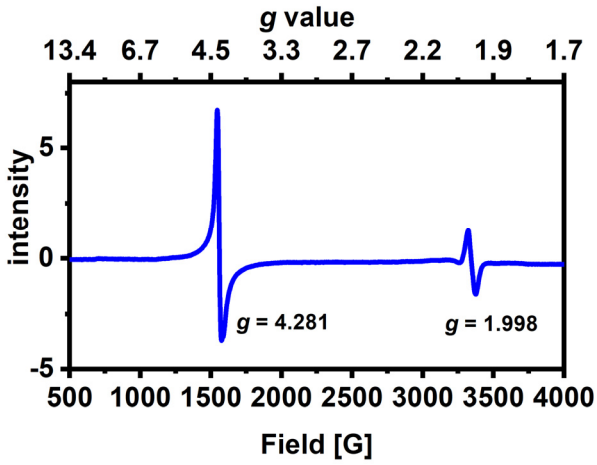

Figure S19. X-band EPR spectrum of the self-decay product of **2** (1 mM) at 12.16 K

Table S6. Comparison of the second-order rate constants k_2 for O-atom transfer and C-H activations (and rate constants k_2' normalized to the number of equivalent H atoms) and KIE values obtained for the C-H activation reactions of **2** with different substrates at -70 °C and their respective C-H bond dissociation energies (BDE), ionization energies (IE) and pK_a values.

Substrate	BDE[a] [kcal/mol]	IE[b] [eV]	pK_a[b]	k_2 (k_2') [$M^{-1}s^{-1}$]	KIE	Product [d]
1,3-CHD	74,3	8,25	35	102 (25.6)[c]		
Xanthene	75,2	7,65	30	1.7 (0.84)[c]	2.1	Xanthone (0.4 eq)
1,4-CHD	76	8,82	-	51 (12.8)[c]		Benzene (0.5 eq)
DHA	76,3	-	30,1	0.81 (0.20)	1.3	Anthracene (0.35 eq)
Fluorene	82,2	7,91	22,6	0.096 (0.048)		
Indene	83	8,14	20,1	0.15 (0.075)		
Ethylbenzene	85,4	8,77	-	0,83 (0.42)	53	Acetophenone (0.2 eq)
Toluene	89,7	8,82	43	0.057 (0.019)	7.3	
Thioanisole	-	-	-	4.41		
PPh_3	-	-	-	too fast		

[a] Values taken from SI reference [28]. [b] Values taken from SI reference [29]. [c] Values calculated for -70°C from experimental values determined at -90 °C using van't Hoff equation. [d] equivalents of the products indicated in respect to the amount of **2** employed in the reaction.

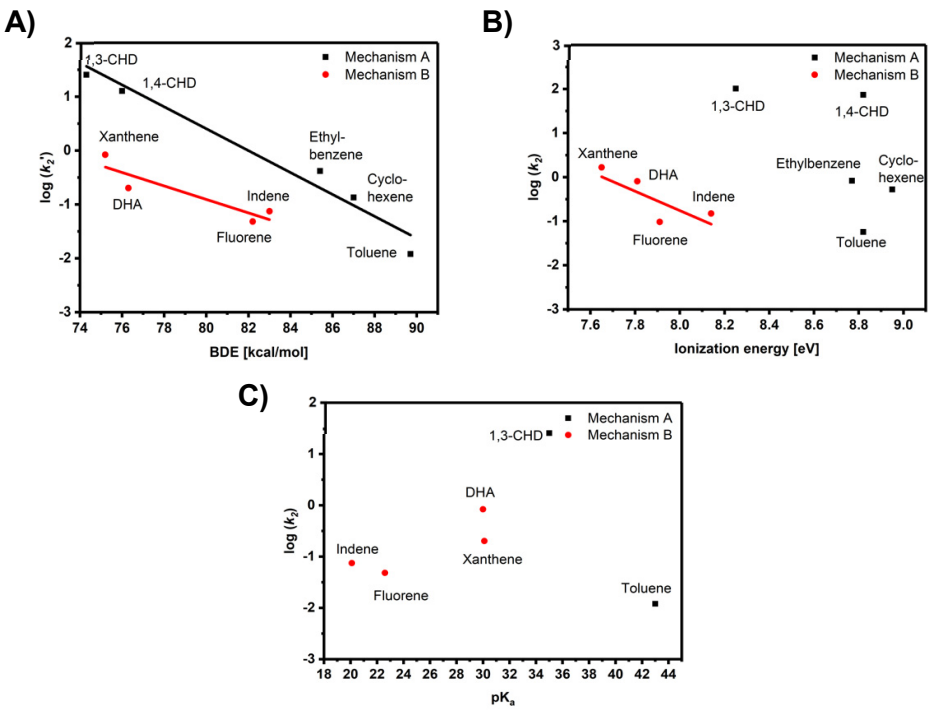

Figure S20. A) Plot of the logarithms of the second-order rate constants k_2' (k_2 values normalized to the number of equivalent H atoms) vs the C-H bond dissociation energies of the substrates for the reactions of several substrates with **2** in CH_2Cl_2 (values measured at -70 °C or recalculated for -70 °C via van't Hoff equation if measured at different temperature); spots are coloured in black and red and fitted by two different trend lines indicating two different reaction mechanisms A (black) and B (red); B) Plot of the logarithms of the rate constants k_2' vs the ionization energies (IE) of the substrates; C) Plot of the logarithms of the rate constants k_2 vs the pK_a values of the substrates.

SUPPORTING INFORMATION

Table S7. Comparison of the reaction rate constants k_2' (normalized to the number of equivalent H atoms) for the C-H activation reaction of **2** and the highly reactive intermediates (TMCO)Fe^{IV}=O, (Me_3NTB)Fe^{IV}=O and (TQA)Fe^{IV}=O towards a selection of substrates.

Substrate	**2**	**(TMCO) Fe^{IV}=O[30]**	**(Me_3NTB) Fe^{IV}=O[31]**	**(TQA) Fe^{IV}=O[32]**
1,3-CHD	$2.0 \cdot 10^2$ [a]			
Xanthene	6.7 [a]			
1,4-CHD	$1.0 \cdot 10^2$ [a]		$7.8 \cdot 10^2$	
DHA	1.6 [b]	Too fast [a]	$2.4 \cdot 10^2$	
Fluorene	0.38 [b]			
Indene	0.6 [b]			
Ethylbenzene	3.3 [b]	0.10 [c]	0.75	1.1
Toluene	0.43 [b]	0.0044 [c]	0.16	0.21
Cyclohexane	-	0.0008 [d]	0.0020	0.0030
Thioanisole	35 [b]			
PPh_3	too fast [a]			

k_2' values at –40 °C were calculated from the values measured at [a] –90 °C; [b] –70 °C; [c] –60 °C; [d] –50 °C. It is considered that the rate becomes half for reduction of temperature by 10 °C.

References

[1] G. M. Sheldrick, University of Göttingen, Germany, **2002**.
[2] G. Sheldrick, *Acta Crystallographica Section A* **2015**, *71*, 3-8.
[3] G. Sheldrick, *Acta Crystallographica Section C* **2015**, *71*, 3-8.
[4] C. B. Hubschle, G. M. Sheldrick, B. Dittrich, *J. Appl. Crystallogr.* **2011**, *44*, 1281-1284.
[5] P. B. Gütlich, E.; Trautwein, A. X., *Mössbauer Spectroscopy and Transition Metal Chemistry*, Springer Verlag, Berlin, Heidelberg, **2011**.
[6] D. Kass, T. Corona, K. Warm, B. Braun-Cula, U. Kuhlmann, E. Bill, S. Mebs, M. Swart, H. Dau, M. Haumann, P. Hildebrandt, K. Ray, *Journal of the American Chemical Society* **2020**, *142*, 5924-5928.
[7] H. Dau, P. Liebisch, M. Haumann, *Analytical and Bioanalytical Chemistry* **2003**, *376*, 562-583.
[8] J. J. Rehr, J. J. Kas, F. D. Vila, M. P. Prange, K. Jorissen, *Physical Chemistry Chemical Physics* **2010**, *12*, 5503-5513.
[9] A. Thangavel, M. Wieliczko, J. Bacsa, C. C. Scarborough, *Inorg. Chem.* **2013**, *52*, 13282-13287.
[10] aD. Macikenas, E. Skrzypczak-Jankun, J. D. Protasiewicz, *Journal of the American Chemical Society* **1999**, *121*, 7164-7165; bJ. Clayden, J. J. A. Cooney, M. Julia, *J. Chem. Soc., Perkin Trans. 1* **1995**, 7-14.
[11] a Baerends, E. J. and co-workers. *ADF2019*, **2019** SCM, Amsterdam. bG. te Velde, F. M. Bickelhaupt, E. J. Baerends, C. Fonseca Guerra, S. J. A. van Gisbergen, J. G. Snijders, T. Ziegler, *J. Comput. Chem.* **2001**, *22*, 931-967.
[12] M. Swart, F. M. Bickelhaupt, *J. Comput. Chem.* **2008**, *29*, 724-734.
[13] aE. Van Lenthe, E. J. Baerends, *J. Comput. Chem.* **2003**, *24*, 1142-1156; bD. P. Chong, E. Van Lenthe, S. Van Gisbergen, E. J. Baerends, *J. Comput. Chem.* **2004**, *25*, 1030-1036.
[14] S. K. Wolff, *Int. J. Quantum Chem* **2005**, *104*, 645-659.
[15] M. Swart, *Chem. Phys. Lett.* **2013**, *580*, 166-171.
[16] A. Klamt, G. Schüürmann, *Journal of the Chemical Society, Perkin Transactions 2* **1993**, 799-805.
[17] M. Swart, E. Rösler, F. M. Bickelhaupt, *Eur. J. Inorg. Chem.* **2007**, *2007*, 3646-3654.
[18] aB. B. Averkiev, D. G. Truhlar, *Catalysis Science & Technology* **2011**, *1*, 1526-1529; bJ. E. M. N. Klein, B. Dereli, L. Que, C. J. Cramer, *Chem. Commun.* **2016**, *52*, 10509-10512.
[19] E. v. Lenthe, E. J. Baerends, J. G. Snijders, *The Journal of Chemical Physics* **1993**, *99*, 4597-4610.
[20] aM. Franchini, P. H. T. Philipsen, L. Visscher, *J. Comput. Chem.* **2013**, *34*, 1819-1827; bA. D. Becke, *The Journal of Chemical Physics* **1988**, *88*, 2547-2553.
[21] M. Álvarez-Moreno, C. de Graaf, N. Lopez, F. Maseras, J. M. Poblet, C. Bo, *J. Chem. Inf. Model.* 2015, 55, 95—103.
[22] M. D. Wilkinson, M. Dumontier, I. J. Aalbersberg, G. Appleton, M. Axton, A. Baak, N. Blomberg, J.-W. Boiten, L. B. da Silva Santos, P. E. Bourne, J. Bouwman, A. J. Brookes, T. Clark, M. Crosas, I. Dillo, O. Dumon, S. Edmunds, C. T. Evelo, R. Finkers, A. Gonzalez-Beltran, A. J. G. Gray, P. Groth, C. Goble, J. S. Grethe, J. Heringa, P. A. C. 't Hoen, R. Hooft, T. Kuhn, R. Kok, J. Kok, S. J. Lusher, M. E. Martone, A. Mons, A. L. Packer, B. Persson, P. Rocca-Serra, M. Roos, R. van Schaik, S.-A. Sansone, E. Schultes, T. Sengstag, T. Slater, G. Strawn, M. A. Swertz, M. Thompson, J. van der Lei, E. van Mulligen, J. Velterop, A. Waagmeester, P. Wittenburg, K. Wolstencroft, J. Zhao, B. Mons, *Scientific Data* **2016**, *3*, 160018.
[23] aJ. C. Price, E. W. Barr, B. Tirupati, J. M. Bollinger, C. Krebs, *Biochemistry* **2003**, *42*, 7497-7508; bJ. M. Bollinger Jr., J. C. Price, L. M. Hoffart, E. W. Barr, C. Krebs, *Eur. J. Inorg. Chem.* **2005**, *2005*, 4245-4254; cP. J. Riggs-Gelasco, J. C. Price, R. B. Guyer, J. H. Brehm, E. W. Barr, J. M. Bollinger, C. Krebs, *Journal of the American Chemical Society* **2004**, *126*, 8108-8109; dS. Sinnecker, N. Svensen, E. W. Barr, S. Ye, J. M. Bollinger, F. Neese, C. Krebs, *Journal of the American Chemical Society* **2007**, *129*, 6168-6179.
[24] J. England, M. Martinho, E. R. Farquhar, J. R. Frisch, E. L. Bominaar, E. Münck, L. Que Jr., *Angew. Chem. Int. Ed.* **2009**, *48*, 3622-3626.
[25] J. England, Y. Guo, K. M. Van Heuvelen, M. A. Cranswick, G. T. Rohde, E. L. Bominaar, E. Münck, L. Que, *Journal of the American Chemical Society* **2011**, *133*, 11880-11883.

[26] D. C. Lacy, R. Gupta, K. L. Stone, J. Greaves, J. W. Ziller, M. P. Hendrich, A. S. Borovik, *Journal of the American Chemical Society* **2010**, *132*, 12188-12190.

[27] aJ.-U. Rohde, J.-H. In, M. H. Lim, W. W. Brennessel, M. R. Bukowski, A. Stubna, E. Münck, W. Nam, L. Que, *Science* **2003**, *299*, 1037; bT. A. Jackson, J.-U. Rohde, M. S. Seo, C. V. Sastri, R. DeHont, A. Stubna, T. Ohta, T. Kitagawa, E. Münck, W. Nam, L. Que, *Journal of the American Chemical Society* **2008**, *130*, 12394-12407.

[28] Y.-R. Luo, *Comprehensive Handbook of Chemical Bond Energies*, CRC Press, Boca Raton, **2007**.

[29] a, *Vol. 69*, National Institute of Standards and Technology, Gaithersburg MD, 20899; bM. K. Goetz, J. S. Anderson, *Journal of the American Chemical Society* **2019**, *141*, 4051-4062.

[30] I. Monte Pérez, X. Engelmann, Y.-M. Lee, M. Yoo, E. Kumaran, E. R. Farquhar, E. Bill, J. England, W. Nam, M. Swart, K. Ray, *Angew. Chem. Int. Ed.* **2017**, *56*, 14384-14388.

[31] M. S. Seo, N. H. Kim, K.-B. Cho, J. E. So, S. K. Park, M. Clémancey, R. Garcia-Serres, J.-M. Latour, S. Shaik, W. Nam, *Chemical Science* **2011**, *2*, 1039-1045.

[32] A. N. Biswas, M. Puri, K. K. Meier, W. N. Oloo, G. T. Rohde, E. L. Bominaar, E. Münck, L. Que, *Journal of the American Chemical Society* **2015**, *137*, 2428-2431.